Deep-red iridium complex with alkyl-functionalized ligands for high-performance phosphorescent organic light-emitting diodes

Yan Bi[1], Shanyong Chen[2,*] , He Zhao[1], and Xiyan Zhang[1,*]

[1] School of Materials Science and Engineering, Changchun University of Science and Technology, Changchun 130022, People's Republic of China

[2] School of Material Science and Engineering, Chongqing University of Arts and Sciences, Yongchuan 402160, People's Republic of China

ABSTRACT

In this work, a novel deep-red (638 nm) iridium complex, Ir(bp3b)$_2$(dend), is developed. This compound exhibits suitable physical properties for a phosphorescent emitter. First, Ir(bp3b)$_2$(dend) and its doped film exhibit balanced charge-transporting ability. Second, methyl and pentyl groups in ligands weaken the intermolecular interaction and endow Ir(bp3b)$_2$(dend) with good film-formation property and low concentration sensitivity. Third, short phosphorescence lifetime (1073.2 ns) indicates that it is relatively easy for triplet exciton to return to the ground state in the form of phosphorescence. Therefore, Ir(bp3b)$_2$(dend)-doped device displays high efficiencies (8.93 cd A^{-1}, 11.57 lm W^{-1}, 15.63%), low roll-off of efficiencies, relatively low concentration sensitivity (from 5 to 10%), long device lifetime (T_{75}: 11,166 h at 100 cd m^{-2}) and very stable electroluminescent spectra (from 1 cd m^{-2} to maximum luminance). This performance is comparable to those of previous record deep-red (635–645 nm) phosphorescent emitters. More importantly, compared with previous record emitters, Ir(bp3b)$_2$(dend) reports more kinds of excellent parameters. Such comprehensive deep-red phosphorescent emitter is rare at present.

1 Introduction

Organic light-emitting diodes (OLEDs) are mainly utilized for display and lighting [1, 2]. At present, the commonly used emitter in commercial OLEDs is iridium(III) complex [3, 4]. To realize high purity full-color display, high-performance deep-blue, blue, geen, yellow, orange, red and deep-red iridium complexes are indispensable. At present, blue, geen, yellow, orange and red iridium complexes have been commercially used. In comparison, high-performance deep-blue and deep-red ($\lambda_{em} \geq 630$ nm) iridium complexes are rare [5]. To solve this problem,

Ⓐ Springer

researchers have carried out many excellent studies [6–10]. In the past decade, a series of new deep-red iridium complexes have been developed [11–23]. However, several aspects need to be improved for deep-red iridium complex. First, more high-performance deep-red iridium complex should be developed because compared with common iridium complexes in other colors, deep-red iridium complex is much less [5–23]. Second, the charge-transporting ability of deep-red iridium complex is usually unbalanced because extending conjugation length or introducing electron-donating group are usually adopted to make the emission color reach deep-red region and this enhances the hole-transporting ability [15, 16, 21, 23]. Third, the roll-off of efficiency should be lowered because the device efficiencies of most of deep-red iridium complexes are not satisfactory [5–23]. Fourth, the concentration sensitivities of most reported deep-red iridium complexes are high [5, 6, 16, 17]. Finally, most of deep-red iridium complexes report limited kinds of excellent parameters and comprehensive emitter is rare at present [5–23]. To solve these problems, developing new molecular structure is essential. Hence, developing novel deep-red iridium complex with balanced charge-transporting ability, high device efficiency and low roll-off of efficiency/concentration sensitivity is still highly desired.

In previous publications [24–27], we observe that steric-hindrance groups in ligands can endow iridium complex with high performance. Hence, in our previous work, we design a green-yellow iridium complex with triphenylsilyl group as steric-hindrance group [2]. Experimental results reveal that triphenylsilyl group can endow iridium complex with favorable intermolecular interactions and then high device performance (high efficiency, low roll-off of efficiency, relatively low concentration sensitivity, long device lifetime and very stable electroluminescent spectra). These works indicate that the introduction of steric-hindrance group into the cyclometalated ligand may be a useful strategy for solving above problems. Steric-hindrance group includes alkyl group and aryl group. Hence, developing deep-red iridium complex with alkyl/aryl-functionalized ligands is worth trying.

Herein, a novel deep-red (638 nm) iridium complex, Ir(bp3b)$_2$(dend), was developed (Scheme 1). 3-(5,6-Bis(3,5-dimethylphenyl)pyrazin-2-yl)-4-methylbenzonitrile (bp3b) and 3,7-diethylnonane-4,6-dione (dend) were adopted as the main ligand and ancillary ligand, respectively [28–31]. Meanwhile, methyl and pentyl groups were introduced into the ligands to adjust the intermolecular interaction. Based on this design, Ir(bp3b)$_2$(dend) exhibited fascinating physical properties: very balanced charge-transporting ability, good film-formation property, short phosphorescence lifetime (1073.2 ns) and low concentration sensitivity. Appropriate physical properties brought about high performance for Ir(bp3b)$_2$(dend)-doped device: high efficiencies (8.93 cd A^{-1}, 11.57 lm W^{-1}, 15.63%), low roll-off of efficiencies, relatively low concentration

Scheme 1 The synthetic procedures of Ir(bp3b)$_2$(dend)
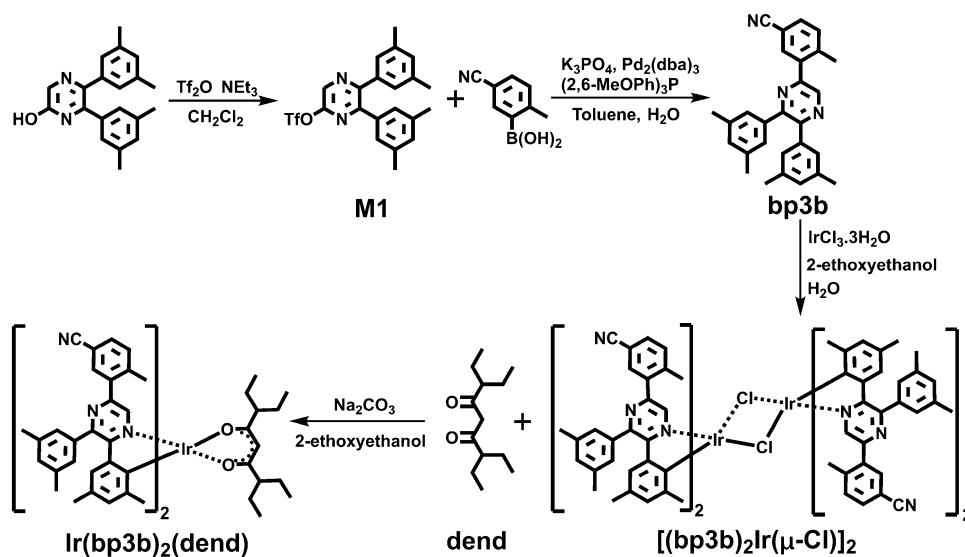
sensitivity (from 5 to 10%), long device lifetime (T_{75}: 11,166 h at 100 cd m^{-2}) and very stable electroluminescent spectra (from 1 cd m^{-2} to maximum luminance). These results indicated that Ir(bp3b)$_2$(dend) was a good and comprehensive deep-red phosphorescent emitter.

2 Experimental section

2.1 General information

All the chemical reagents were purchased from commercial sources and used as received without purification unless otherwise noted. ^{1}H and ^{13}C NMR spectra were measured using an AVANCE 400 MHz spectrometer (Bruker). Mass spectrometry were characterized by Shimazu LCMS2020 instrument. Elemental analyses were performed on a flash EA 1112 spectrometer. Ultraviolet–visible (UV–vis) absorption spectra were tested using a Hitachi U-3900 spectrophotometer. A Horiba FluoroMax-4 spectrophotometer spectrometer was used for fluorescence spectra. Thermal gravimetric analysis (TGA) and differential scanning calorimetry (DSC) characteristics were determined by TA Q600 thermogravimeter and NETZSCH DSC204 instrument using the heating rate of 10 °C min^{-1} under nitrogen atmosphere. The cyclic voltammetry has been investigated by electrochemical workstation, the working electrode was a platinum electrode, the reference electrode was an Ag electrode, and the counter electrode was a platinum wire. The photoluminescence quantum yields (PLQYs) were measured with the Yokohama C9920-02G assay system.

Geometry optimizations of ground state of the materials were carried out using Becke-Lee-Young-Parr composite exchange correlation (B3LYP) methods. The Los Alamos Lab (LANL2DZ) basis sets were employed for the Ir atom and "Double-α" quality basis sets were employed for the ligands (6-31G*). Time dependent density functional theory (TD-DFT) was used to obtain the vertical excitation energy. The geometry of the lowest triplet-state was examined by optimizing the structure at the spin-unrestricted B3LYP level, and the phosphorescence emission energies of the models were calculated by TD-DFT method. All calculations have been performed using Gaussian 16 package.

2.2 OLED fabrication and characterization

All devices were fabricated on indium tin oxide (ITO) substrate. ITO substrate was treated with Plasma for 5 min before being transferred to a vacuum deposition chamber. Then, organic and inorganic layers were evaporated sequentially through a shadow mask at the pressure of 5.0×10^{-4} Pa. After the device was finished, its current–voltage-luminance (J-V-L) characteristics, electroluminescent (EL) spectra and brightness were measured with s system containing a Keithley 2400 and spectrograph PR-670. All measurements were carried out under nitrogen conditions at room temperature.

2.3 Synthesis

2.3.1 5,6-Bis(3,5-dimethylphenyl)pyrazin-2-yl trifluoromethanesulfonate (M1)

To a three-necks round-bottom flask, 5,6-bis(3,5-dimethylphenyl)pyrazin-2-ol (39.1 g, 128.5 mmol), triethylamine (36.6 mL, 263.3 mmol) and dichloromethane (650 mL) were added. After degassed throughly, trifluoromethanesulfonic anhydride (33.2 mL, 197.3 mmol) was added slowly below – 20 °C. Then, the mixture was stirred at room temperature for 26 h. After reaction finished, distilled water (440 mL) and hydrochloric acid (44 mL) were added. The mixture was stirred for 20 min and then extracted by dichloromethane (900 mL × 3) for three times. The organic phase was washed by saturated sodium bicarbonate solution and then dried by anhydrous sodium sulfate. The solution passed through a buchner funnel which was filled with silica gel. Finally, the organic solvent was removed by rotary evaporation and an oily product (56 g) was obtained. Yield: nearly 100%. ^{1}H NMR (400 MHz, DMSO-d_6, δ): 9.00 (s, 1H), 7.07 (d, J = 4 Hz, 2H), 7.03 (s, 2H), 7.00 (s, 2H), 2.20 (d, J = 4 Hz, 12H). ^{13}C NMR (400 MHz, CDCl$_3$, δ): 24.76, 83.70, 127.77, 129.51, 133.80, 133.92, 135.55, 136.27, 137.70. HR-MS: 437.11434 [M + H]$^+$ (calcd: 436.11).

2.3.2 3-(5,6-Bis(3,5-dimethylphenyl)pyrazin-2-yl)-4-methylbenzonitrile (bp3b)

To a three-necks round-bottom flask, 5,6-bis(3,5-dimethylphenyl)pyrazin-2-yl trifluoromethanesulfonate (56 g, 128.3 mmol), (5-cyano-2-methylphenyl)boronic acid

(24.81 g, 154.1 mmol), tripotassium phosphate (95.4 g, 449.4 mmol), tris(dibenzylideneacetone)dipalladium (1.2 g, 1.31 mmol), tris(2,6-dimethoxyphenyl)phosphine (2.3 g, 5.20 mmol), toluene (1000 mL) and distilled water (100 mL) were added. After being degassed throughly, the mixture was refluxed for 8 h. The reaction was monitored by thin layer chromatography (TLC). If the reaction was not complete, additional catalytic agent (about 0.25 equivalent) was added. After reaction finished, distilled water (1000 mL) was added and then the mixture was stirred for 20 min. The organic phase was separated and the aqueous phase was extracted by toluene (300 mL × 3). After dried by anhydrous sodium sulfate, the solution passed through a buchner funnel which was filled with silica gel. The organic solvent was removed by rotary evaporation and then petroleum ether (2000 mL) was added. The mixture was stirred and refluxed for 15 h. After being cooled to room temperature, the mixture was filtrated and the filter cake was washed by petroleum ether. Finally, after being diried in an oven (60 °C) for 6 h, the product was obtained. Yield: 82%. ^{1}H NMR (400 MHz, DMSO-d_6, δ): 8.90 (s, 1H), 8.09 (s, 1H), 7.88 (dd, J = 4 Hz, 1H), 7.62 (d, J = 8 Hz, 1H), 7.08 (d, J = 8 Hz, 4H), 7.03 (s, 2H), 2.52 (s, 3H), 2.20 (d, J = 4 Hz, 12H). ^{13}C NMR (400 MHz, CDCl$_3$, δ): 21.08, 21.21, 110.34, 118.62, 127.40, 127.45, 130.44, 131.92, 132.11, 133.58, 137.60, 137.64, 138.00, 138.11, 141.16, 142.28, 149.64, 151.43, 152.19. HR-MS: 404.21177 [M + H]$^+$ (calcd: 403.20).

2.3.3 [(bp3b)$_2$Ir(μ-Cl)]$_2$

To a three-necks round-bottom flask, bp3b ligand (4.2 g, 10.41 mmol), iridium trichloride (1.67 g, 4.74 mmol), 2-ethoxyethanol (42 mL) and distilled water (14 mL) were added. After being degassed for three times, the mixture was stirred at 120 °C for 24 h under nitrogen atmosphere. After being cooled to room temperature, the mixture was filtrated and the filtrate cake was washed by methanol. Finally, the product was dried in an oven (50 °C). Yield: 73%.

2.3.4 Ir(bp3b)$_2$(dend)

To a three-necks round-bottom flask, [(bp3b)$_2$Ir(μ-Cl)]$_2$ (3.6 g, 1.74 mmol), sodium carbonate (1.8 g, 16.98 mmol) and N, N-dimethylformamide (50 mL) were added. After being degassed for three times, 3,7-diethylnonane-4,6-dione (1.4 g, 6.59 mmol) was added under nitrogen. The mixture was stirred at 140 °C for 4 h. After reaction finished, the solvent

was removed by rotary evaporation and the residue was dissolved in dichloromethane. The solution passed through a buchner funnel which was filled with silica gel. The organic solvent was removed by rotary evaporation and the obtained solid was dissolved in dichloromethane again. Then, methanol was added into the solution and product precipitated. The mixture was filtrated and filtrate cake was washed by methanol. After being dried in an oven at 60 °C, relatively pure sample (1.5 g) was obtained. Yield: 36%. The product was further purified by vacuum sublimation. Sublimation yield: 76%. ^{1}H NMR (400 MHz, CDCl$_3$, δ): 8.43 (s, 2H), 7.64 (d, J = 4 Hz, 2H), 7.58 (d, J = 4 Hz, 1H), 7.56 (d, J = 4 Hz, 1H), 7.36–7.40 (m, 5H), 7.17 (s, 2H), 6.85 (s, 2H), 6.51 (s, 2H), 5.10 (s, 1H), 2.46 (s, 7H), 2.39 (s, 11H), 1.97 (s, 6H), 1.77–1.84 (m, 2H), 1.54 (s, 1H), 1.44 (s, 6H), 1.17–1.39 (m, 9H), 0.40 (t, J = 8 Hz, 6H), 0.32 (t, J = 8 Hz, 6H). ^{13}C NMR (400 MHz, CDCl$_3$, δ): 11.80, 20.71, 20.90, 21.30, 24.00, 25.93, 26.65, 54.79, 100.64, 110.15, 118.39, 126.81, 127.30, 129.87, 131.14, 131.77, 131.92, 132.24, 133.18, 137.00, 138.67, 139.47, 142.51, 144.36, 144.49, 145.66, 147.18, 152.77, 160.94, 191.07. MS: 1210 [M + H]$^+$ (calcd: 1209.53). Anal. Calcd for C$_{69}$H$_{72}$IrN$_6$O$_2$: C 68.52, H 6.00, N 6.95; found: C 68.49, H 6.01, N 6.97.

3 Results and discussion

3.1 Synthesis and thermal properties

Ir(bp3b)$_2$(dend) was prepared through four steps (Scheme 1). First, hydroxyl group was activated by trifluoromethanesulfonic anhydride. Then, bp3b ligand was prepared through a Suzuki reaction. Sequentially, chloridebridged dimer was obtained from bp3b ligand and iridium trichloride. Finally, 3,7-diethylnonane-4,6-dione (dend) reacted with chloridebridged dimer to provide Ir(bp3b)$_2$(dend). Further purification was carried out by sublimation and electronic grade product was fully characterized by ^{1}H NMR, ^{13}C NMR, mass spectra and element analysis (Figs. S1–S9).

bp3b ligand possesses two coordination sites. One is at the ortho-position of 4-methylbenzonitrile group and another one is at the meta-position of 4-methylbenzonitrile group. Obviously, the steric hindrance at ortho-position site is much higher than that at meta-position site. From the point of steric hindrance,

Fig. 1 **a** TGA and **b** DSC thermograms of Ir(bp3b)$_2$(dend)
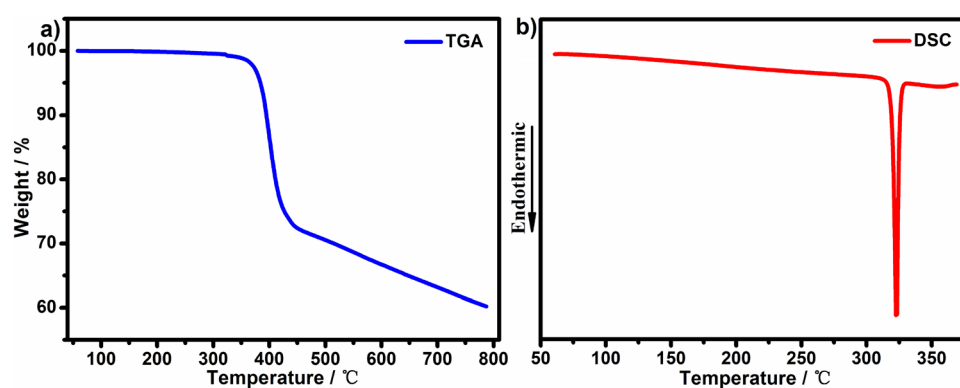
iridium will mainly coordinate at the meta-position site. Meanwhile, in previous patents [28–31], a Japan company reports similar iridium complexes. Those complexes also display meta-position coordination structure. Hence, we think the product in this work is also meta-position coordination structure (Scheme 1).

The thermal property of Ir(bp3b)$_2$(dend) was investigated by thermogravimetric analysis (TGA) and differential scanning calorimetry (DSC) (Fig. 1; Table 1). The decomposition temperature (T_d) (corresponding to 5% weight loss) of Ir(bp3b)$_2$(dend) was determined to be 384 °C, indicating that Ir(bp3b)$_2$(dend) possessed high thermal stability. No glass transition was detected. Meanwhile, no crystal was obtained through common growth methods. This was probably because the alkyl groups in ligands weakened the intermolecular interaction and prevented the molecular crystallization. This characteristic was beneficial for preparing uniform amorphous film which could promote the device efficiency and lifetime.

3.2 Electrochemical properties and theoretical calculation

Cyclic voltammetry (CV) measurement was utilized to investigate the electrochemical property of Ir(bp3b)$_2$(dend) (Fig. 2b). Reversible oxidation behavior was observed and no reduction wave was detected. From the oxidation wave, its highest occupied molecular orbital (HOMO) energy level was determined to be − 5.27 eV. Meanwhile, its lowest unoccupied molecular orbital (LUMO) energy level was estimated to be − 3.20 eV from its HOMO and absorption spectra. The appropriate HOMO and LUMO energy levels might help the carrier injection from charge-transporting layer to emitting layer.

The orbital spatial distribution, frontier orbital energy levels and energy level compositions of Ir(bp3b)$_2$(dend) were examined by density functional theory (DFT) calculations (Fig. 2a and Table S1). The HOMO and LUMO orbitals corresponded to 280 and 281 orbitals. From the calculation results of 280 and 281 orbitals, it could be seen that the HOMO orbital uniformly distributed on iridium atom and three

Table 1 Physical properties of Ir(bp3b)$_2$(dend)

Compound	$T_d{}^a$ [°C]	$\lambda_{abs}{}^b$ [nm]	$\lambda_{em}{}^c$ [nm]	FWHM^c [nm]	Φ^d [%]	τ^c [ns]	HOMO^e/LUMO^f [eV]	$E_g{}^g$ [eV]
Ir(bp3b)$_2$(dend)	384	206, 219, 290, 366, 421, 503	640	58.3	56.2	1073.2	−5.27/−3.20	2.07

$^a T_d$: decomposition temperature corresponding to 5% weight loss

^{b}Measured in CH$_2$Cl$_2$ solution (10^{-5} M) at room temperature

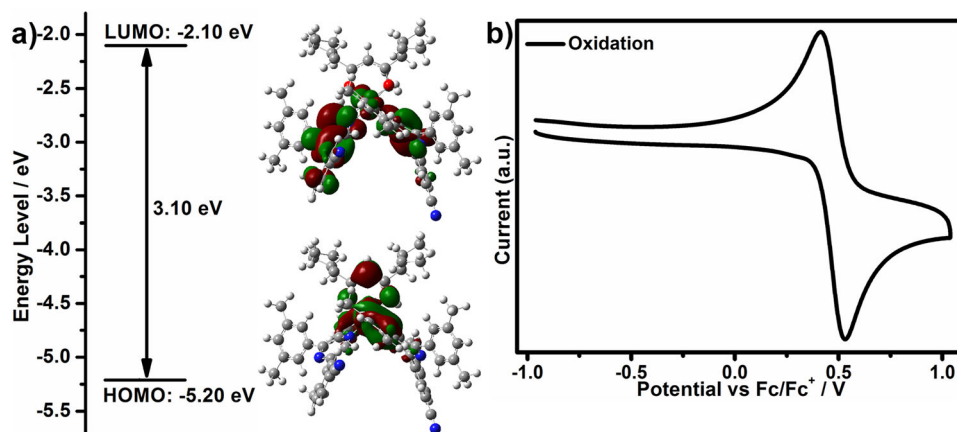^{c}Measured in degassed CH$_2$Cl$_2$ solution (10^{-5} M) at room temperature

^{d}Measured in degassed CH$_2$Cl$_2$ solution (10^{-5} M) at room temperature

^{e}HOMO was obtained from the peaks of oxidation curve

^{f}LUMO was calculated from HOMO and E_g (LUMO = HOMO + E_g)

$^g E_g$ was estimated from the right onset of absorption spectra (E_g = 1240/λ_{abs})

ligands (d orbital of Ir: 28.13%; π orbital of bp3b-1: 19.92%; π orbital of bp3b-2: 28.79%; π orbital of dend: 23.16%), while the LUMO orbital mainly located on π^* orbital of bp3b ligands (Ir: 2.22%; bp3b-1: 74.82%; bp3b-2: 22.70%; dend: 0.26%). Meanwhile, the theoretical HOMO and LUMO energy levels of Ir(bp3b)$_2$(dend) were calculated to be -5.20 eV and -2.10 eV, respectively. The excited states of Ir(bp3b)$_2$(dend) were studied by time-dependent density functional theory (TD-DFT) calculations (Table S2). The lowest excitation energy and maximum absorption wavelength were 2.41 eV and 513 nm, respectively, corresponding to the transition from 280 to 281 molecular orbitals. According to Table S1, this transition was from d orbital of iridium to π^* orbital of bp3b ligand, from π orbital of bp3b and dend ligands to π^* orbital of bp3b ligand. Hence, this transition mainly included metal–ligand charge transfer (MLCT), ligand-ligand charge transfer (LLCT) and intra-ligand charge transfer (ILCT) transitions.

Besides singlet excited state, the triplet excited state (T_1, T_2, T_3) of Ir(bp3b)$_2$(dend) was also calculated under triplet-state geometric configuration by TD-DFT calculations (Table S3). For phosphorescence emission, it mainly arose from the transition from T_1 state to ground state. For Ir(bp3b)$_2$(dend), its T_1 state mainly corresponded to the transition from 280 molecular orbital to 281 molecular orbital (proportion: 97.1%). According to Table S1, the transition for T_1 was mainly from d orbital of iridium to π^* orbital of bp3b ligand, from π orbital of bp3b and dend ligands to π^* orbital of bp3b ligand. Hence, MLCT, LLCT and ILCT transitions had contribution on the

phosphorescence emission. Meanwhile, the energy of T_1 state was calculated to be 1.49 eV and the maximum phosphorescence wavelength was 831 nm.

3.3 Photophysical properties

The absorption (10^{-5} M) and photoluminescence (PL) spectra (10^{-4}, 10^{-5}, 10^{-6} M) of Ir(bp3b)$_2$(dend) in degassed dichloromethane solution are exhibited in Fig. 3a. There were six absorption peaks (206, 219, 290, 366, 421, 503 nm). According to the calculation results and previous publications [5–8], the strong absorption peaks below 350 nm should be assigned to the ILCT transition, while the absorption from 350 to 600 nm should be ascribed to the MLCT, ILCT and ligand-ligand charge transfer (LLCT) transitions facilitated by the spin–orbit coupling of iridium atom. From the absorption spectra, the energy gap (E_g) was determined to be 2.07 eV.

Ir(bp3b)$_2$(dend) displayed deep-red emission in dichloromethane (Fig. 3a). At the concentrations of 10^{-6}, 10^{-5} and 10^{-4} M, the emission peaks were 640.4, 640.3 and 642.2 nm, respectively, while the full width at half maximum (FWHM) were 55.5, 58.3 and 60.5 nm, respectively. The emission peak almost had no change with the variation of solution concentration, indicating that Ir(bp3b)$_2$(dend) exhibited low concentration sensitivity. Figure 3b showed the transient photoluminescence decay characteristic of Ir(bp3b)$_2$(dend). From this curve, the photoluminescence lifetime of Ir(bp3b)$_2$(dend) was determined to be 1073.2 ns. For deep-red ($\lambda_{em} \geq 630$ nm) iridium complex, this lifetime was short [5–23]. Finally, the photoluminescence quantum yield (PLQY) of

Fig. 3 **a** Room-temperature UV–Vis absorption (10^{-5} M) and photoluminescence (PL) spectra (10^{-4}, 10^{-5}, 10^{-6} M) of Ir(bp3b)$_2$(dend) in degassed dichloromethane solution. **b** Transient PL decay profile of Ir(bp3b)$_2$(dend) in degassed toluene solution (10^{-5} M) at room temperature
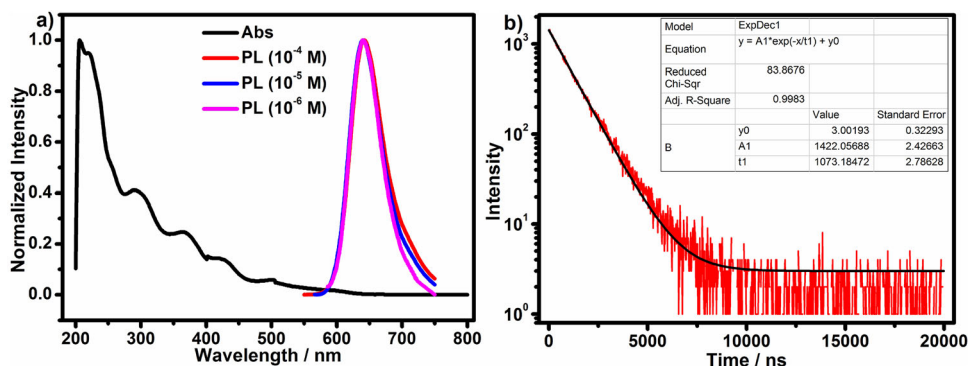
Ir(bp3b)$_2$(dend) in degassed dichloromethane solution (10^{-5} M) was 56.2%.

We also investigated the photophysical properties of doped films (mCP: 5–15% Ir(bp3b)$_2$(dend)) (Fig. S10; Table S4). The absorption and photoluminescence (PL) spectra of these three doped films were almost the same, further revealing that Ir(bp3b)$_2$(dend) exhibited low concentration sensitivity. At the doped concentration of 5%, 10%, 15%, the emission peaks were 644, 645 and 645 nm, respectively, while the FWHMs were 51.6, 58.2 and 58.0 nm, respectively. The PLQYs at 5%, 10%, 15% doped concentrations were 68.6%, 57.0% and 45.5%, respectively, while the photoluminescence lifetime were 449.2, 249.5 and 169.5 ns, respectively.

3.4 Charge-transporting properties

Hole-only and electron-only devices were fabricated to investigate the charge-transporting ability of Ir(bp3b)$_2$(dend) (Fig. 4a). The structure of hole-only device was [ITO/MoO$_3$ (10 nm)/TAPC (20 nm)/Ir(bp3b)$_2$(dend) (100 nm)/TAPC (20 nm)/MoO$_3$ (10 nm)/Al], while the structure of electron-only device was [ITO/Liq (1.5 nm)/TPBi (30 nm)/Ir(bp3b)$_2$(dend) (100 nm)/TPBi (30 nm)/Liq (1.5 nm)/Al]. MoO$_3$ and TPBi could prevent the electron injection and hole-injection, respectively. Therefore, pure hole and electron currents could be realized, respectively. From Fig. 4a, it could be seen that Ir(bp3b)$_2$(dend) was a phosphorescent emitter whose hole- and electron-transporting abilities were balanced. Based on space charge limited current method [32, 33], the hole and electron mobilities of

Ir(bp3b)$_2$(dend) were calculated to be 2.72×10^{-7} cm^2 V^{-1} s^{-1} (0.7 V) and 2.62×10^{-7} cm^2 V^{-1} s^{-1} (0.7 V), respectively. Meanwhile, compared with these two mobilities calculated at low voltage (0.7 V), the mobilities at device's working voltage (2.3–6.0 V) were much higher. Moderate charge-transporting ablility indicated that small methyl and pentyl groups in ligands could only weaken the intermolecular interaction to a certain extent and some intermolecular interactions still existed. Balanced and moderate charge-transporting ability was favorable for realizing high device performance.

To examine the charge-transporting abilities of emitting layers in OLEDs, the hole-only and electron-only devices of mCP host and doped films (mCP: 5–15% Ir(bp3b)$_2$(dend)) were fabricated (Figs. 4b, S11). The structure of hole-only device was [ITO/MoO$_3$ (10 nm)/TAPC (20 nm)/mCP or doped films (100 nm)/TAPC (20 nm)/MoO$_3$ (10 nm)/Al], while the structure of electron-only device was [ITO/Liq (1.5 nm)/TPBi (30 nm)/mCP or doped films (100 nm)/TPBi (30 nm)/Liq (1.5 nm)/Al]. After Ir(bp3b)$_2$(dend) was doped into mCP host, the hole and electron current of doped films were almost the same with those of mCP host (Fig. S11). Meanwhile, with the increase of doped concentration (from 5 to 15%), the hole and electron current of doped films were almost the same (Fig. 4b). These experimental results indicated that Ir(bp3b)$_2$(dend) didn't exhibit hole or electron-trap effect in emitting layer because carrier trap would make the current density of emitting layer decrease and change with the doped concentration [34, 35]. Finally, the hole- and electron-transporting abilities of doped films were not only
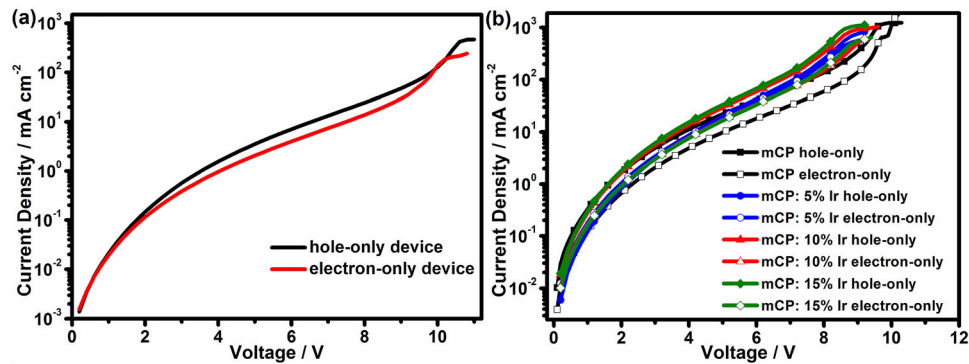
Fig. 4 a Current density versus voltage characteristics of the hole-only and electron-only devices of Ir(bp3b)$_2$(dend). **b** Current density versus voltage characteristics of the hole-only and electron-only devices of mCP host and doped films (mCP: 5–15% Ir(bp3b)$_2$(dend))

high, but also balanced (Fig. 4b). High and balanced charge-transporting ability was beneficial for promoting the device performance.

3.5 Electroluminescent properties

Phosphorescent doped devices were fabricated to examine the luminescent performance of Ir(bp3b)$_2$(dend). The device structure was [ITO/HATCN (15 nm)/TAPC (40 nm)/TCTA (5 nm)/mCP: 5–15% Ir(bp3b)$_2$ (dend) (25 nm)/BAlq (5 nm)/TPBI (40 nm)/LiF (1 nm)/Al] (Device R1 for 5%; Device R2 for 10%; Device R3 for 15%). In these devices, the hole-injection material, hole-transporting material, electron-blocking material, host material, electron-transporting material were dipyrazino [2,3-f:2′,3′-h] quinoxaline-2,3,6,7,10,11-hexacarbonitrile (HATCN), 4,4′-cyclohexylidenebis [N,N-bis (p-tolyl) aniline] (TAPC), 4,4′,4″-tris (carbazol-9-yl)-triphenylamine (TCTA), 1,3-bis-9H-carbazol-9-ylbenzene (mCP) and bis(2-methyl-8-quinolinolato-N1,O8)-(1,1′-biphenyl-4-olato)aluminum (BAlq)/ 1,3,5-tris(1-phenyl-1H-benzimidazol-2-yl)benzene (TPBI) respectively. The molecular structures and their energy levels are shown in Fig. S12. The luminance-voltage-current density (L-V-J) characteristics, current/power/external quantum efficiencies *versus* luminance curves and electroluminescent (EL) spectra are shown in Figs. 5, S13 and Table 2.

These three devices exhibited deep-red emission (638 nm) with Commission International de l'Eclairage (CIE) coordinate of (0.69, 0.30) (Fig. 5d). The full width at half maximum (FWHM) was 56.7 nm. The EL spectra displayed low concentration sensitivity. With the increase of doped concentration from 5 to

15%, the EL spectra were the same (Fig. 5d). These devices showed high efficiency (Fig. 5b–c; Table 2). For devices R1, R2 and R3, their maximum current ($\eta_{c.max}$), power ($\eta_{p.max}$) and external quantum ($\eta_{ext.max}$) efficiencies were as following: 8.88 cd A^{-1}, 11.50 lm/W, 15.52% for device R1; 8.93 cd A^{-1}, 11.57 lm W^{-1}, 15.63% for device R2; 8.25 cd A^{-1}, 10.69 lm W^{-1}, 14.43% for device R3. From 5 to 10%, the device efficiencies were almost the same, further revealing the relatively low concentration sensitivity of Ir(bp3b)$_2$(dend). From 10 to 15%, the device efficiencies decreased and the reduction ratios of current, power and external quantum efficiencies were 7.61%, 7.61% and 7.68%, respectively. Obviously, between 5 and 10%, the device efficiencies were almost not affected by the doped concentration, indicating that in this range, the doped concentration didn't need precise control. This characteristic was favorable for practical application. The decreased device efficiency from 10 to 15% might be related with the decrease of PLQY. At 10% and 15% doped concentrations, the PLQYs of doped films were 57.0% and 45.5%, respectively. Meanwhile, the roll-off of efficiencies were also low. From 100 to 1000 cd m^{-2}, the roll-off ratios of current efficiencies were 2.59% for device R1, 2.58% for device R2. From 1000 to 5000 cd m^{-2}, the roll-off ratios of current efficiencies were 9.03% for device R1, 9.77% for device R2. Finally, at different driving voltage, the EL spectra exhibited high stability. From 2.3 to 6.0 V (luminance: 1 cd m^{-2} to maximum luminance), the EL spectra had no change (Figs. 5e, f, S13).

Besides the device efficiency, device lifetime was also important for practical application. Hence, the

Fig. 5 **a** Luminance-voltage-current density (L-V-J) curves of devices R1, R2, R3. **b** Current efficiency–luminance-power efficiency (CE-L-PE) curves of devices R1, R2, R3. **c** External quantum efficiency–luminance curves of devices R1, R2, R3. **d** EL spectra of devices R1, R2, R3 at the luminance of 100 cd m^{-2}. **e** EL spectra of device R2 at different voltages (from 2.3 to 6.0 V; interval: 0.1 V). **f** Normalized EL spectra of device R2 at different voltages (from 2.3 to 6.0 V; interval: 0.1 V)
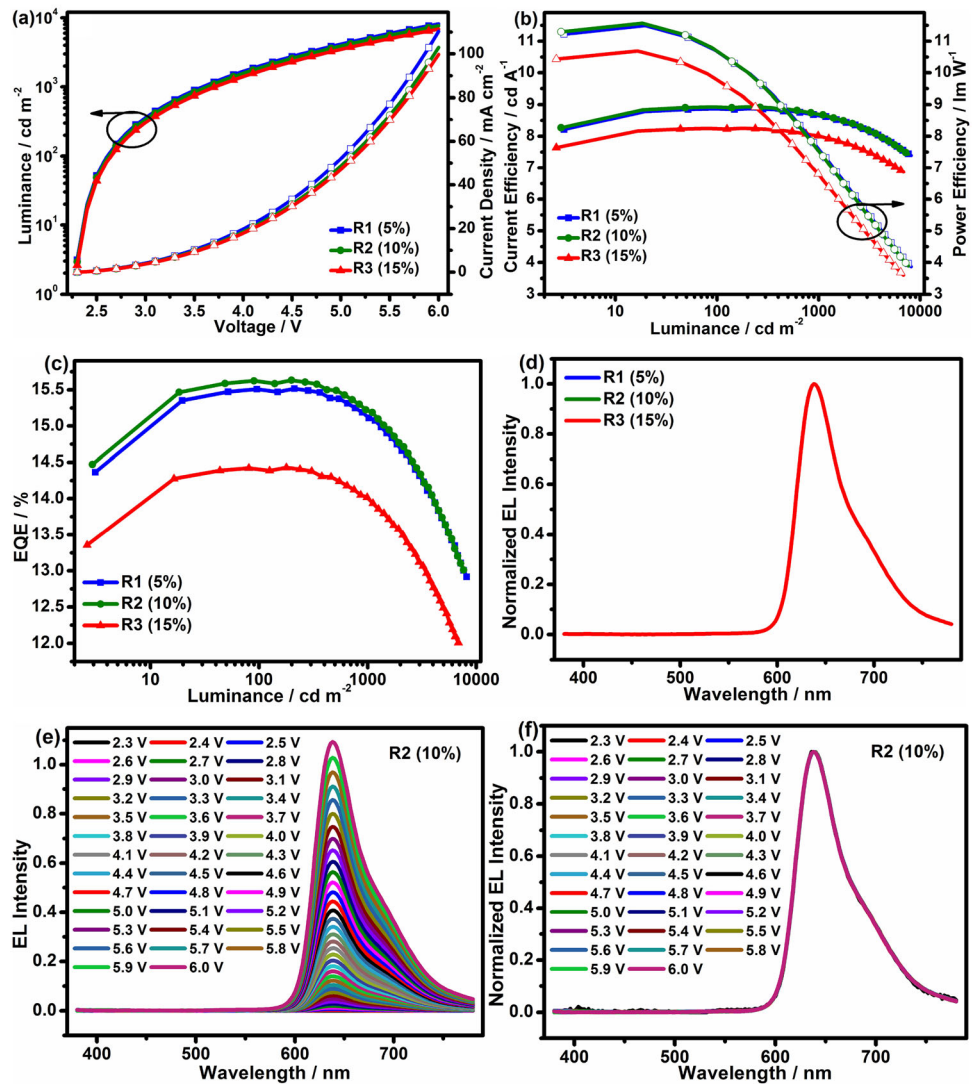

Table 2 The electroluminescent performance of Ir(bp3b)$_2$(dend)-doped devices

Device	V_{on}[a] [V]	L_{max}[b] [cd m^{-2}]	η_c[c] [cd A^{-1}]	η_p[c] [lm W^{-1}]	η_{ext}[c] [%]	CIE (x,y)[d]	FWHM[d] [nm]	T_{75}[e] [h]
R1(5%)	2.3	8146	8.88, 8.87, 8.64, 7.86	11.50, 10.72, 7.54, 4.75	15.52, 15.51, 15.11, 13.73	638 (0.69, 0.30)	56.7	10,020
R2(10%)	2.3	7651	8.93, 8.93, 8.70, 7.85	11.57, 10.79, 7.59, 4.65	15.63, 15.62, 15.22, 13.74	638 (0.69, 0.30)	56.7	11,166
R3(15%)	2.3	6852	8.25, 8.23, 8.02, 7.14	10.69, 9.57, 6.81, 4.08	14.43, 14.42, 14.02, 12.49	638 (0.69, 0.30)	56.7	9179

[a]V_{on}: Voltage recorded at 1 cd m^{-2}

[b]L_{max}: Maximum luminance. η_c: Current efficiency. η_p: Power efficiency. η_{ext}: External quantum efficiency

[c]In the order of maximum, then values at 100, 1000 and 5000 cd m^{-2}

[d]Measured at 100 cd m^{-2}; FWHM: full width at half maximum

[e]The device operation lifetime (75% initial luminance) at 100 cd m^{-2}

lifetimes of devices R1, R2, R3 were measured (Fig. S14). High initial luminance (L_0) was utilized to accelerate the measurements. The conversion formula was as following: T_{75} (L_1) = T_{75} (L_0) × $(L_0/L_1)^{1.7}$ [36–38]. Here, T_{75} was the operation lifetime when the luminance decreased to 75% initial luminance, L_1 and L_0 represented the objective and experimental initial luminance, respectively. For devices R1, R2, R3, the experimental initial luminances were 699, 721, 689 cd m^{-2}, respectively, while the T_{75} values at their experimental initial luminances were 367.5, 388.5, 345.0 h, respectively. According to the calculation formula, the lifetimes of devices R1, R2, R3 at objective initial luminance (100 cd m^{-2}) were 10,020, 11,166, 9179 h, respectively. For deep-red phosphorescent emitter, these lifetimes were long [5–23]. Long device lifetime indicated that Ir(bp3b)$_2$(dend) was a stable emitter.

For external quantum efficiency (EQE), its value could be calculated by the following formula: EQE = $\gamma \times \eta_r \times \eta_p \times \eta_e$. Here, γ was the balance factor of hole-electron recombination in emitting layer, η_r was the ratio of triplet exciton generation, η_p was the ratio of triplet exciton which returned to the ground state in the form of phosphorescence, η_e was the ratio of light which could be out of the device. For Ir(bp3b)$_2$(dend)-doped device, it exhibited high efficiencies, low roll-off of efficiencies and relatively low concentration sensitivity. The good performance should be attributed to the following three reasons. First, both Ir(bp3b)$_2$(dend) and emitting layers possessed high and balanced charge-transporting abilities which brought about high γ. Second, short phosphorescence lifetime (1073.2 ns) meant it was relatively easy for triplet exciton to return to the ground state in the form of phosphorescence. Third, methyl and pentyl groups in ligands weakened the intermolecular interaction and prevented the close packing of molecules. Hence, uniform amorphous film could be easily prepared and the concentration sensitivity was lowered.

Besides above reasons, we also investigated whether the orientation of Ir(bp3b)$_2$(dend) in emitting layer had contribution on the high efficiency of devices. Variable-angle spectroscopic ellipsometry (VASE) measurement was carried out. According to previous publications [39–41], the orientation of transition dipole moment can be quantified by an orientation order parameter S which is defined by the ordinary and extraordinary extinction coefficients k_o and k_e, respectively:

$$S = \frac{k_e^{max} - k_o^{max}}{k_e^{max} + 2k_o^{max}},$$

where k_o^{max} and k_e^{max} are the ordinary (horizontal direction) and extraordinary (vertical direction) extinction coefficients at the peak of the band attributed to the transition dipole moment, respectively. Generally, $S = -0.5$, $S = 0$ and $S = 1$ represent completely horizontal, random orientation (isotropic distribution) and completely vertical, respectively. Meanwhile, the horizontal dipole ratio (R_h) can be calculated by the following equation [39]:

$$R_h = \frac{h}{h + v} = \frac{2(1 - S)}{3}$$

According to previous publication [39], the theoretical maximum EQE of OLEDs increases as the horizontal dipole ratio exceeds 67%. The ordinary and extraordinary refractive indices (n_o and n_e) and extinction coefficients (k_o and k_e) of doped film (mCP: 10% Ir(bp3b)$_2$(dend)) were measured by variable angle spectroscopic ellipsometry (Fig. S15). Within the whole test range, n_o is higher than n_e, revealing that Ir(bp3b)$_2$(dend) was anisotropic and horizontally oriented in emitting layer [39]. The k_e^{max} and k_o^{max}, were 0.3770 and 0.4578, respectively. Hence, S and R_h were calculated to be -0.06251 and 70.8%. R_h exceeded 67%. Therefore, the orientation of Ir(bp3b)$_2$(dend) in emitting layer had contribution on the high efficiency of devices by promoting the light output efficiency.

The device performance of previous record deep-red (635–645 nm) phosphorescent emitters and Ir(bp3b)$_2$(dend) was compared (Table 3). For deep-red emitter, larger emission peak would bring about lower device efficiency and it was appropriate to compare those deep-red emitters whose emission peak differences were less than 5 nm. For phosphorescent emitters between 635 and 645 nm, the device efficiency of Ir(bp3b)$_2$(dend) was comparable to those of previous record deep-red (635–645 nm) phosphorescent emitters [14–23]. For practical application, the emitter should be comprehensive and possess many excellent parameters (device efficiency, roll-off of efficiency, concentration sensitivity, device lifetime, spectra stability, etc.) simultaneously. In this respect, compared with previous record emitters, Ir(bp3b)$_2$(dend) reported more kinds of excellent parameters (Table 3). Such comprehensive emitter was rare at present.

Table 3 The performance comparison between previous high-performance deep-red ($\lambda_{em:}$ 635–645 nm) phosphorescent emitters and Ir(bp3b)$_2$(dend) in devices with single host and single luminescent layer

Compound	CE [cd A^{-1}]	PE [lm W^{-1}]	EQE	CIE[a]	Roll-off[b]	Concentration sensitivity[c]	Device lifetime[d] [h]	Spectra stability[e]	References
(f2piq)$_2$Ir(dipba)	/	10.4	16.7%	644(0.69,0.31)	Moderate	High	/	/	[14]
SOIrOPh	12.8	9.14	25.8%	640(0.68,0.30)	Low	Very high	T_{50} = 470 h (500 cd m^{-2})	/	[16]
(4tfmpq)$_2$Ir(dipdtc)	9.51	7.86	15.30%	641(0.68,0.31)	Low	/	/	/	[18]
Ir-2	11.75	9.90	14.96%	636(0.67,0.33)	Low	/	/	/	[19]
(piq)$_2$Ir(tmhd)	/	/	16.3%	634	Low	/	/	/	[22]
Ir3	8.7	6.6	10.1%	637(0.69,0.31)	High	/	/	/	[23]
Ir4	9.8	7.7	12.1%	638(0.69,0.31)	High	/	/	/	[23]
Ir(bp3b)$_2$(dend)	8.93	11.57	15.63%	638(0.69, 0.30)	Low	Low	T_{75} = 11,166 h (100 cd m^{-2})	Stable	This work

CE current efficiency, *PE* power efficiency, *EQE* external quantum efficiency

[a]The maximum peaks and Commission International de l'Eclairage coordinates of electroluminescent spectra

[b]Roll-off: Roll-off of current efficiency from 10 to 1000 cd m^{-2}

[c]Concentration sensitivity: The variation of current efficiency at different doped concentrations. [d]The lifetime obtained at 50% or 75% initial luminance

[e]Spectra stability: The spectra stability from 1 to several thousands cd m^{-2}

4 Conclusions

In summary, we developed a novel deep-red iridium complex, Ir(bp3b)$_2$(dend). This material exhibited balanced charge-transporting ability, good film-formation property, short phosphorescence lifetime and low concentration sensitivity. Based on these physical properties, Ir(bp3b)$_2$(dend)-doped device displayed high performance which was comparable to those of previous record deep-red (635–645 nm) phosphorescent emitters. More importantly, Ir(bp3b)$_2$(dend) was more comprehensive than these emitters. This work not only provides a novel high-performance deep-red iridium complex, but also exhibits an efficient strategy for developing comprehensive phosphorescent emitter.

Author contributions

SC and XZ designed and directed the research. YB synthesized the target compound and characterized its physical property. HZ fabricated the OLED device and collected the device data. All authors contributed to the general discussion. All authors have approved the final version of the manuscript.

Data availability

The data that support the findings of this study are available within the article.

Declarations

Conflict of interest The authors declare that they have no conflict of interest.

Supplementary Information: The online version contains supplementary material available at http s://doi.org/10.1007/s10854-022-09074-z.

References

1. P. Wang, J.S. Yu, S.Y. Chen, H. Yu, X.W. Yan, Y.W. Guan, J.L. Chen, L. Li, Dyes Pigm. **183**, 108744 (2020)
2. Y. Bi, J.C. Wei, S.Y. Chen, H. Zhao, X.Y. Zhang, J. Phys. Chem. C **125**, 24671 (2021)
3. C.H. Fan, P.P. Sun, T.H. Su, C.H. Cheng, Adv. Mater. **23**, 2981 (2011)
4. C.F. You, D.H. Liu, M.B. Zhu, J.T. Yu, B. Zhang, Y. Liu, Y.F. Wang, W.G. Zhu, J. Mater. Chem. C **8**, 7079 (2020)
5. N. Altinolcek, A. Battal, M. Tavasli, J. Cameron, W.J. Peveler, H.A. Yu, P.J. Skabara, Synthetic Met. **268**, 116504 (2020)
6. X.J. Liu, S.M. Wang, B. Yao, B.H. Zhang, C.L. Ho, W.Y. Wong, Y.X. Cheng, Z.Y. Xie, Org. Electron. **21**, 1 (2015)
7. Z.R. Hao, K. Zhang, P. Wang, X.M. Lu, Z.Y. Lu, W.G. Zhu, Y. Liu, Inorg. Chem. **59**, 332 (2020)
8. N. Su, H.Q. Yang, Y.X. Zheng, Z.X. Chen, New J. Chem. **43**, 8722 (2019)
9. R.H. Liu, D.X. Ma, L. Duan, J. Mater. Chem. C **8**, 14766 (2020)
10. G.Z. Lu, J.W. Yao, Z.X. Chen, D.G. Ma, C.L. Yang, J. Mater. Chem. C **8**, 1391 (2020)
11. H.U. Kim, H.J. Jang, W. Choi, M. Kim, S. Park, T. Park, J.Y. Lee, K.S. Bejoymohandas, J. Mater. Chem. C **7**, 4143 (2019)
12. H.U. Kim, S. Sohn, W. Choi, M. Kim, S.U. Ryu, T. Park, S. Jung, K.S. Bejoymohandas, J. Mater. Chem. C **6**, 10640 (2018)
13. L. Zhao, S.M. Wang, J.H. Lu, J.Q. Ding, L.X. Wang, J. Mater. Chem. C **5**, 9753 (2017)
14. G.M. Li, P. Li, X.M. Zhuang, K.Q. Ye, Y. Liu, Y. Wang, A.C.S. Appl, Mater. Int. **9**, 11749 (2017)
15. G.Z. Lu, Q. Zhu, L. Liu, Z.G. Wu, Y.X. Zheng, L. Zhou, J.L. Zuo, H.J. Zhang, A.C.S. Appl, Mater. Int. **11**, 20192 (2019)
16. Y.H. Sun, X.L. Yang, Z. Feng, B.A. Liu, D.K. Zhong, J.J. Zhang, G.J. Zhou, Z.X. Wu, A.C.S. Appl, Mater. Int. **11**, 26152 (2019)
17. B.Y. Liang, Z.S. Yu, X.M. Zhuang, J.X. Wang, J.B. Wei, K.Q. Ye, Z.L. Zhang, Y. Liu, Y. Wang, Chem. Eur. J. **26**, 4410 (2020)
18. G.Z. Lu, N. Su, H.Q. Yang, Q. Zhu, W.W. Zhang, Y.X. Zheng, L. Zhou, J.L. Zuo, Z.X. Chen, H.J. Zhang, Chem. Sci. **10**, 3535 (2019)
19. Y. Ding, D. Liu, J.Y. Li, H.T. Li, H.Y. Ma, D.L. Li, R. Niu, Dyes Pigm. **179**, 108405 (2020)
20. Y.M. Jing, F.Z. Wang, Y.X. Zheng, J.L. Zuo, J. Mater. Chem. C **5**, 3714 (2017)
21. G.Z. Lu, X.K. Li, L. Liu, L. Zhou, Y.X. Zheng, W.W. Zhang, J.L. Zuo, H.J. Zhang, J. Mater. Chem. C **7**, 3862 (2019)
22. S.Y. Baek, S.Y. Kwak, S.T. Kim, K.Y. Hwang, H. Koo, W.J. Son, B. Choi, S. Kim, H. Choi, M.H. Baik, Nat. Commun. **11**, 2292 (2020)
23. Y.M. Jing, Y.X. Zheng, RSC Adv. **7**, 37021 (2017)
24. V.K. Rai, M. Nishiura, M. Takimoto, S. Zhao, Y. Liu, Z. Hou, Inorg. Chem. **51**, 822 (2012)
25. H. Cao, H. Sun, Y. Yin, X. Wen, G. Shan, Z. Su, R. Zhong, W. Xie, P. Li, D. Zhu, J. Mater. Chem. C **2**, 2150 (2014)
26. V.K. Rai, M. Nishiura, M. Takimoto, Z. Hou, J. Mater. Chem. C **2**, 5317 (2014)
27. Q. Mei, L. Liu, J. Yang, X. Jiang, S. Ye, L. Zhang, B. Tong, Dyes Pigm. **199**, 110075 (2022)
28. Y. Tomoya, Y. Hideko, K. Yuta, W. Takeyoshi, S. Satoshi, US2021214381A1 (2021)
29. Y. Tomoya, Y. Eiko, K. Yuta, W. Gokichi, S. Tetsushi, CN113105508A (2021)
30. Y. Tomoya, Y. Eiko, K. Yuta, W. Gokichi, S. Tetsushi, JP2021175719A (2021)
31. Y. Tomoya, T. Masatoshi, Y. Hideko, WO2022018577A1, (2022).
32. L.J. Wang, G.J. Nan, X.D. Yang, Q. Peng, Q.K. Li, Z.G. Shuai, Chem. Soc. Rev. **39**, 423 (2010)
33. V. Coropceanu, J. Cornil, D.A. da Silva, Y. Olivier, R. Silbey, J.L. Bredas, Chem. Rev. **107**, 926 (2007)
34. K. Udagawa, H. Sasabe, C. Cai, J. Kido, Adv. Mater. **26**, 5062 (2014)
35. H. Sasabe, H. Nakanishi, Y. Watanabe, S. Yano, M. Hirasawa, Y.J. Pu, J. Kido, Adv. Funct. Mater. **23**, 5550 (2013)
36. J. Lin, Y. Wang, P. Gnanasekaran, Y.C. Chiang, C.C. Yang, C.H. Chang, S.H. Liu, G.H. Lee, P.T. Chou, Y. Chi, S.W. Liu, Adv. Funct. Mater. **27**, 1702856 (2017)
37. T. Fleetham, Y.L. Ji, L. Huang, T.S. Fleetham, J. Li, Chem. Sci. **8**, 7983 (2017)

38. G. Cheng, S.C.F. Kui, W.H. Ang, M.Y. Ko, P.K. Chow, C.L. Kwong, C.C. Kwok, C.S. Ma, X.G. Guan, K.H. Low, S.J. Su, C.M. Che, Chem. Sci. **5**, 4819 (2014)

39. X.Y. Li, J.Y. Zhang, Z.F. Zhao, L.D. Wang, H.N. Yang, Q.W. Chang, N. Jiang, Z.W. Liu, Z.Q. Bian, W.P. Liu et al., Adv. Mater. **30**, 1705005 (2018)

40. A.K. Pal, S. Krotkus, M. Fontani, C.F.R. Mackenzie, D.B. Cordes, A.M.Z. Slawin, I.D.W. Samuel, E. Zysman-Colman, Adv. Mater. **30**, 1804231 (2018)

41. M. Liu, R. Komatsu, X.Y. Cai, K. Hotta, S. Sato, K.K. Liu, D.C. Chen, Y. Kato, H. Sasabe, S. Ohisa et al., Chem. Mater. **29**, 8630 (2017)